ADVANCED FUNCTIONAL MATERIALS
www.afm-journal.de

Methanol-Facilitated Surface Reconstruction Catalysts for Near 200% Faradaic Efficiency in a Coupled System

Qing Xia, Chengkai Jin, Yu Lun Huang, Yanjie Zhai, Wenkai Han, Jie Wu, Chuan Xia, Chun Che Lin, Xunhua Zhao,* and Xiao Zhang**

The coupling of the carbon dioxide reduction reaction (CO_2RR) and methanol oxidation reaction (MOR) holds great promise for the energy-efficient production of $HCOO^-$. However, anode catalysts' limited selectivity (<80%) and stability (<15 h) have impeded electron utilization and $HCOO^-$ production rates. To overcome it, copper-copper(I) oxide-copper(II) oxide nanowires (Cu—CuO—Cu_2O NWs) catalysts have been developed, which exhibit exceptional performance in promoting the MOR with a faradic efficiency of nearly 100% at commercially viable current densities, and long stability over 100 h at 100 mA cm^{-2}. Interestingly, the unique structure of the catalysts, when exposed to methanol, facilitates a transition from Cu/CuO to Cu_2O. This phenomenon promotes the MOR while inhibiting the competitive oxygen evolution reaction (OER). By coupling the anodic reaction with cathodic CO_2 reduction, the system demonstrates exceptional performance in $HCOO^-$ production, achieving an overall faradic efficiency of nearly 200% at 100 mA cm^{-2} with a low cell voltage of 2.382 V. Techno-economic analysis indicates that the production costs of HCOOH are ≈US$0.37 and 0.35 kg^{-1} at 100 and 150 mA cm^{-2}, respectively, significantly lower than those associated with traditional electrochemical methods.

1. Introduction

Formate ($HCOO^-$) is an industrially important chemical, widely employed in animal feed (34%) and leather tanning (32%). The market for the compound currently is ≈$6 billion and exhibits a steady growth trajectory in terms of demand (**Figure 1a**).[1] The traditional chemical process for $HCOO^-$ production relies heavily on the carbonylation of methanol, followed by hydrolysis of methyl formate ($HC(O)OCH_3$), which accounts for 80% of the total production.[2] However, this process requires to necessitate considerable energy investment, predominantly fueled by fossil-based sources, which in turn exerts a significant environmental toll.[3] Additionally, the feedstock of $HC(O)OCH_3$ holds a much higher value ($1.6 kg^{-1}) compared to $HCOO^-$/HCOOH ($0.5 kg^{-1}), thereby rendering the process less economically viable.[1a,4]

Q. Xia, Y. Zhai, W. Han, J. Wu, X. Zhang
Department of Mechanical Engineering
Research Institute for Advanced Manufacturing
The Hong Kong Polytechnic University
Kowloon, Hung Hom 999077, Hong Kong
E-mail: xiao1.zhang@polyu.edu.hk

Q. Xia, Y. Zhai, J. Wu, X. Zhang
Research Institute for Smart Energy
The Hong Kong Polytechnic University
Kowloon, Hung Hom 999077, Hong Kong

C. Jin, X. Zhao
Key Laboratory of Quantum Materials and Devices of Ministry of Education
School of Physics Southeast University
Nanjing 211189, China
E-mail: xhzhao@seu.edu.cn

Y. L. Huang, C. C. Lin
Institute of Organic and Polymeric Materials
National Taipei University of Technology
Taipei 106, Taiwan
E-mail: cclin0530@mail.ntut.edu.tw

C. Xia
School of Materials and Energy
University of Electronic Science and Technology of China
Chengdu, Sichuan 610000, P. R. China

C. C. Lin
Research and Development Center for Smart Textile Technology
National Taipei University of Technology
Taipei 106, Taiwan

X. Zhang
Shenzhen Research Institute
The Hong Kong Polytechnic University
Shenzhen 518057, China

The ORCID identification number(s) for the author(s) of this article can be found under https://doi.org/10.1002/adfm.202314596

DOI: 10.1002/adfm.202314596

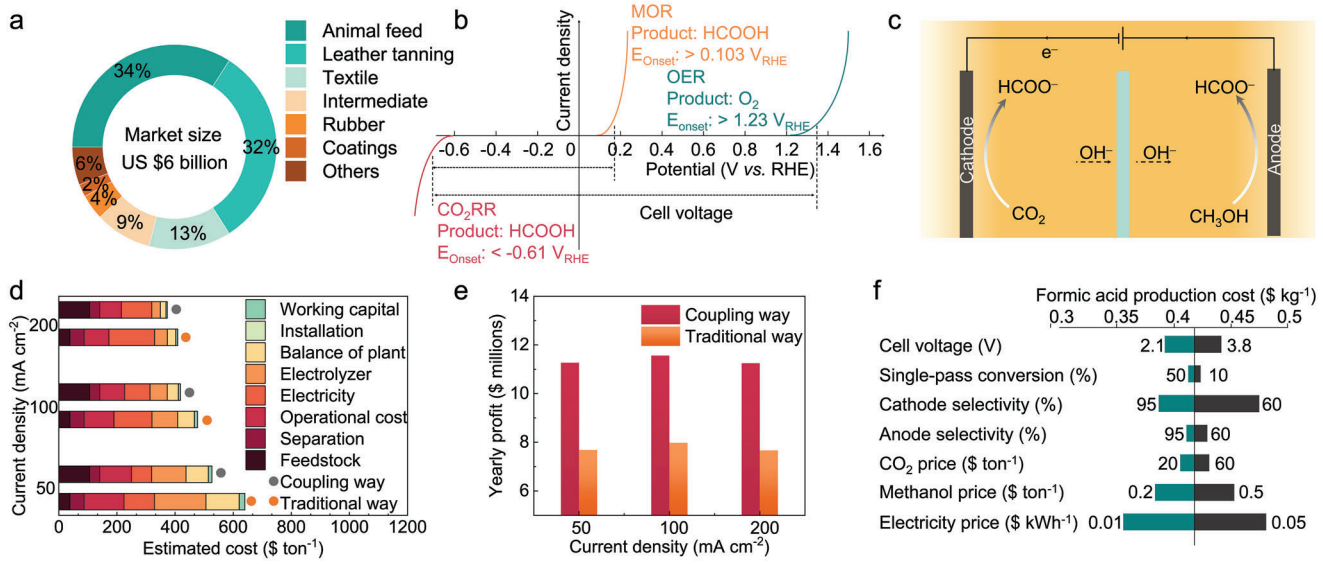

Figure 1. Preliminary comparison of traditional methods and electrochemically coupled methods for $HCOO^-$ production. a) Application field and market size of $HCOO^-$. The data are obtained online, https://www.oxfa.eu/en/markets/. b) Onset potential comparison for CO_2RR, MOR, and OER under standard experimental conditions. c) Schematic diagram of electrocatalytic CO_2RR coupled with MOR under alkaline conditions to produce $HCOO^-$. d) TEA of the electrochemical coupling process to estimate the HCOOH production cost at different current densities. e) Yearly profit comparison between the traditional and coupling methods with a similar condition. f) Production cost changes for various parameters for HCOOH production, the values shown in the figures indicate each optimistic and pessimistic parameter.

Conversion of the low-value carbon resources, powered by clean energy, has emerged as a promising alternative to producing $HCOO^-$.[5] One representative process is the electrochemical reduction of carbon dioxide (CO_2) to $HCOO^-$, which has been widely investigated recently.[6] However, the overall performance for the production of $HCOO^-$ is strongly influenced by the anodic reactions and the overall cell configurations. For example, the practical implementation faces challenges as the anodic reaction often encompasses oxygen evolution reaction (OER), which suffers from high overpotential and only produces low-value of oxygen gas (O_2),[7] limiting electron utilization efficiency and the overall energy efficiency of the electrolysis cell. Therefore, there is an urgent need to develop efficient anodic coupled reactions that can generate $HCOO^-$ while simultaneously decreasing the energy input.

One promising candidate for this purpose is the conversion of methanol (CH_3OH), the simplest monohydric alcohol, which holds relatively low economic value (200–$400 ton^{-1}) and can be derived from diverse sources like woods, agricultural residues, energy crops, and municipal solid wastes.[8] The methanol oxidation reaction (MOR) offers a favorable option as it delivers four-electrons per molecule and exhibits an equilibrium potential of 0.103 V versus a standard hydrogen electrode, significantly lower than the OER potential of 1.23 V (Figure 1b).[9] Moreover, the MOR can produce $HCOO^-$ that can be coupled with the CO_2 reduction reaction (CO_2RR), potentially doubling electron utilization and enhancing production rates by 50% (Figure 1c).[10] To evaluate the economic feasibility of this possible strategy, we conducted a preliminary techno-economic analysis (TEA), assuming moderate reaction performance (Note S1 and Table S1 (Supporting Information), the HCOOH is thought as the final product for the TEA analysis in this paper). The analysis underscores the potential of this coupled method to significantly reduce the production costs of HCOOH compared to traditional CO_2RR with OER (Figure 1d). The projected annual profit is roughly 50% higher than traditional CO_2RR (Figure 1e), with optimized conditions potentially reducing costs further to $0.35 kg^{-1} (Figure 1f), highlighting the economic viability of this strategy. However, the current implementation of industrial-scale production for the electrochemical $HCOO^-$ production faces a significant obstacle mainly due to the low selectivity, activity, and stability of the anode catalyst toward the desired four-electron MOR at a commercial current density, which needs nearly 1.6 V to achieve 100 mA cm^{-2} and can only keep stable below 15 h.[11] Such high voltages intensify competition from the OER, resulting in the low production rate of $HCOO^-$. From the point of view of molecular activation, the cleavage of the strong C—H bond of intermediate species, $^*CH_3O$ and $^*CH_2O$, is the main hindrance to the overall reaction and serves as the rate-determining step for various catalysts.[12] To address this issue, designing a catalyst to achieve low C—H bond energy is vital for the successful industrial-scale deployment of this strategy.

In this study, we have successfully developed a highly efficient catalyst comprising copper-copper(I) oxide-copper(II) oxide nanowires (Cu—CuO—Cu_2O NWs) catalysts. The catalyst not only decreases the dehydrogenation energy of intermediates but also alters the rate-determining step to the $^*CH_3OH \rightarrow {}^*CH_3O$ through a methanol-assisted catalyst surface restructuring process. The unique structure of Cu—CuO—Cu_2O NWs catalysts enables them to exhibit exceptional performance in promoting $HCOO^-$ production, achieving a remarkable faradaic efficiency of nearly 100% across a wide current density range of 100–600 mA cm^{-2}, as well as excellent long-term stability over 100 h

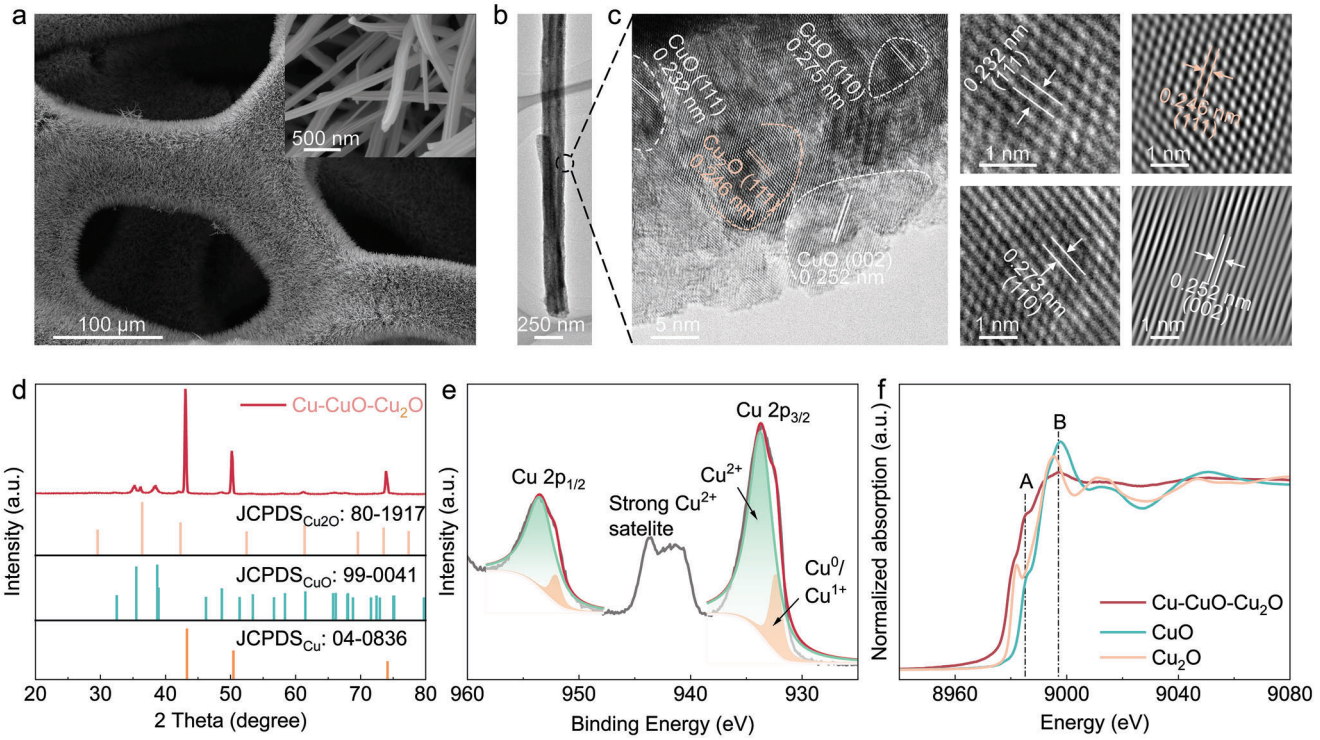

Figure 2. Characterizations of the Cu—CuO—Cu_2O NWs catalysts. a) Scanning electron microscope (SEM) image of the prepared Cu—CuO—Cu_2O NWs catalyst. The inset is the magnified SEM image of the Cu—CuO—Cu_2O NWs catalyst. b) TEM and c) HRTEM image of the prepared Cu—CuO—Cu_2O NWs catalysts. d) XRD pattern of the Cu—CuO—Cu_2O NWs as well as standard XRD patterns of Cu_2O, CuO, and Cu. e) High-resolution Cu 2p XPS spectra for the NWWS. f) Normalized Cu K-edge XANES spectra of the NWWS, Cu_2O, and CuO. The NWWS is the nanowire without Cu substrate.

at a current density of 100 mA cm^{-2}. A noteworthy aspect of our findings is the unexpected phenomenon we discovered, where methanol not only serves as a reactant but also assists in the reconstruction of the catalyst surface, which amplifies the four-electron MOR and suppresses the undesired OER. By coupling this efficient anode reaction with CO_2RR, we achieved highly efficient $HCOO^-$ production at a low voltage with an impressive faradaic efficiency of nearly 200% at a commercially viable current density. Our design allowed for a production rate of 2.62 mmol cm^{-2} h^{-1} (28.93 kg m^{-2} day^{-1}) and a low production cost for HCOOH at ≈\$0.37 kg^{-1} when operating at 100 mA cm^{-2}, potentially yielding an annual profit of up to \$14 million at the same current densities.

2. Results and Discussion

2.1. Catalyst Design and Preparation

For the formation of $HCOO^-$ through the four-electron MOR reaction, two crucial steps typically take place. The initial step occurs on the catalyst surface, preferably utilizing materials based on transition metals,[13] where the O-H bond of the adsorbed methanol CH_3OH_{ad}) is cleaved. The subsequent step involves the dehydrogenation of $^*CH_3O$ and $^*CH_2O$. In this process, the oxygen atom on the catalyst surface plays a critical role in reducing the energy barrier for breaking the C—H bond, thereby promoting the four-electron MOR.[13b,14] Inspired by this mechanism, we focused on the Cu-based oxide materials, specifically Cu oxides grown directly on Cu foam, to initiate the reaction. This approach offers two advantages for the MOR: first, it enables efficient electron transfer due to solid conjunction between substrates and active compositions, enhancing the MOR kinetics; secondly, it ensures resistance to catalyst deterioration during the electrolysis process, thus ensuring long-term stability.

The Cu-based catalyst was prepared through a two-step process, i.e., electrodeposition of $Cu(OH)_2$ onto Cu foam in KOH solution followed by annealing in an Ar atmosphere (see details in methods). During the electrodeposition process, the surface of Cu foam first underwent oxidation, forming Cu^{2+}, which immediately reacted with OH^- to form Cu-$Cu(OH)_2$ nanowire (Figures S1 and S2 and Note S2, Supporting Information). After electrodeposition, the sample was then heat-treated to convert $Cu(OH)_2$ to Cu-based oxides. As shown in **Figure 2**a,b, the catalyst morphology is maintained after annealing, and the nanowires are uniformly grown on the Cu foam substrate. The size of the nanowire falls within specific ranges, with 3–8 μm in length and 100–300 nm in diameter, and Cu and O elements are uniformly distributed throughout the nanowire structure (Figure S3, Supporting Information). The high-resolution transmission electron microscopy (HRTEM) image of the nanowire reveals a mixture of (110), (111), and (002) planes of CuO, along with the (111) plane of Cu_2O. Notably, the (002) plane of CuO predominantly occupies the catalyst surface (Figure 2c). The X-ray diffraction (XRD) pattern showed typical peaks of Cu, CuO, and Cu_2O, further confirming the formation of CuO and Cu_2O on the Cu substrate

(Figure 2d). Therefore, we name the catalyst as Cu—CuO—Cu_2O NWs.

The surface chemical state of the nanowire without substrate (defined as NWWS) was then investigated using X-ray photoelectron spectroscopy (XPS). The XPS analysis showed that only Cu and O elements were present in the sample, with no other impurities detected (Figure S4a, Supporting Information). Moreover, the Cu 2p spectrum revealed that the Cu predominantly existed in the divalent state on the catalyst surface with characteristic peaks at 933.7 and 953.5 eV (Figure 2e),[15] consistent with the HRTEM results. Owing to the closely similar binding energy values of Cu^{1+} and Cu^0 peaks in the Cu 2p spectra, which complicates their distinction, we further analyzed the Cu LM2 peak to accurately determine the chemical valence states of Cu (see Figure S4b, Supporting Information). The peaks at 917.7 eV and 913.0 eV were identified as Cu^{1+} and Cu^0, respectively, indicating the coexistence of both Cu^{1+} and metallic Cu^0 in the nanowires. The O 1s spectrum shows two main peaks, one at 529.4 eV can be assigned to the Cu-O bond coming from the CuO and Cu_2O, and another peak at 531.1 eV can be assigned to O vacancies (Figure S4b, Supporting Information).[16] Furthermore, the distinct electron paramagnetic resonance (EPR) signal (g = 2.003) observed in the Cu—CuO—Cu_2O NWs also confirms the presence of oxygen vacancies, which may change the structure of the Cu_2O and CuO. To gain further insight into the electronic and local geometric structural properties of the NWWS, the Cu K-edge X-ray absorption spectra (XAS) were conducted. As shown in Figure 2f, it displayed lower adsorption energy compared to the reference sample Cu_2O, suggesting the presence of Cu^0 within the nanowire. In addition, the characteristic peaks A and B, situated between the characteristic peaks of Cu_2O and CuO, further supported the mixed valence of Cu^{2+} and Cu^+. The Fourier transform (FT) k^3-weighted $\chi(k)$ function of the extended X-ray absorption fine structure (EXAFS) spectrum for the NWWS is depicted in Figure S5a (Supporting Information). The first main peak is discernible at 1.47 Å, aligning with the primary feature peak for the bulk Cu_2O.[17] Another notable peak is at 1.90 Å, attributable to the Cu–O distances in defective CuO.[18] This peak supersedes the main feature peak of the bulk CuO at 1.57 Å, resulting from structural changes induced by the presence of O vacancies in CuO. The structural alteration leads to a configuration where four O atoms are bonded with Cu (as depicted in Figure S5b, Supporting Information), which is also confirmed by the XPS results (Figure S4b, Supporting Information). Significantly, an additional peak at 2.60 Å is apparent, representing the Cu−Cu coordination within the Cu metal of the nanowire.[19]

2.2. Intrinsic Catalytic Performance of Cu—CuO—Cu_2O NWs for Methanol Oxidation

We then evaluated the intrinsic electrocatalytic performance of the Cu—CuO—Cu_2O NWs toward methanol oxidation by employing a standard three-electrode H-type cell under ambient temperature and pressure. In the presence of a 1.0 M KOH + 1.0 M CH_3OH electrolyte, the catalyst demonstrated a low potential of 1.38 V versus RHE at a current density of 100 mA cm^{-2} (**Figure** 3a,b), which was 288 mV lower than that required in a 1.0 M KOH electrolyte to reach the same current density. Notably, an increase in CH_3OH concentration in the electrolyte resulted in a corresponding reduction in the potential necessary to maintain the same current density (Figures S6 and S7, Supporting Information), suggesting a high activity of the Cu—CuO—Cu_2O NWs for MOR instead of the OER. The decreased Tafel slopes in electrolytes containing CH_3OH further corroborate this, showing more facile MOR kinetics compared to OER (Figure S8, Supporting Information). Remarkably, the Cu—CuO—Cu_2O NWs catalyst exhibited an exceptionally low onset potential of 1.0 V in both electrolytes, which is much lower compared with previous reports (1.2–1.4 V).[20] We postulate that this behavior may be attributed to the catalyst reconstruction during the electrocatalytic MOR (will be discussed in the following section). The lower potential required of the Cu—CuO—Cu_2O NWs catalyst to drive the reaction compared with recent high-performance MOR catalysts under similar testing conditions (Figure 3c) further underscores the outstanding activity of our catalyst.[10,20a,21]

Then electrochemical impedance spectroscopy (EIS) and electrochemical surface area (ECSA) measurements were employed to reveal the interfacial charge transfer kinetics and active surface area of the Cu—CuO—Cu_2O NWs. As shown in Figure S9 (Supporting Information), the Cu—CuO—Cu_2O NWs demonstrates a remarkably low impedance (less than 0.6 Ω) when immersed in electrolytes, facilitating a rapid electron transfer for the MOR. This exceptional conductivity is attributed to the presence of metallic Cu within the nanowire structure. The ECSA was evaluated by measuring the double-layer capacitance (C_{dl}) from cyclic voltammograms (CVs) at different scan rates. As illustrated in Figure S10b (Supporting Information), the Cu—CuO—Cu_2O NWs deposited on the carbon paper indicate an ECSA with a value of 0.059 mF cm^{-2}.

The $HCOO^-$ selectivity at the anode is key in determining the overall $HCOO^-$ production rate in a full electrochemical reactor. Therefore, the anodic $HCOO^-$ product produced by the Cu—CuO—Cu_2O NWs catalyst was collected and quantified by proton nuclear magnetic resonance (^1H NMR) spectroscopy (Figures S11 and S12, Supporting Information). We found that the Cu—CuO—Cu_2O NWs delivered a maximum $HCOO^-$ faradaic efficiency (FE) of 99% at 50 mA cm^{-2} and maintained a high FE plateau over 93% across a wide current density ranging from 10 to 600 mA cm^{-2} (Figure 3d). Moreover, our Cu—CuO—Cu_2O NWs catalyst can efficiently work at high current densities to deliver an industrial-relevant production rate for $HCOO^-$ product. By increasing current densities to 800 mA cm^{-2} and 1 A cm^{-2}, a small number of gas bubbles appeared on the catalyst surface (Figure S13, Supporting Information), which may be due to the possible occurrence of OER. Despite this, the FE_{HCOO-} remained consistently above 85%, and the $HCOO^-$ production rate reached an impressive value of 8.23 mmol cm^{-2} h^{-1} at 1 A cm^{-2}. The carbon-13 nuclear magnetic resonance (^{13}C NMR) was then conducted on the electrolyte before and after 2 h of operation at 100 mA cm^{-2} to examine the possibility of excessive methanol oxidation leading to CO_2 formation. As shown in Figure 3e, a small peak that arises from the CO_3^{2-} (168.3 ppm) was observed before the reaction, likely originating from the absorbed CO_2 by the KOH electrolyte due to air exposure. After the reaction, the CO_3^{2-} signal was still present. However, both

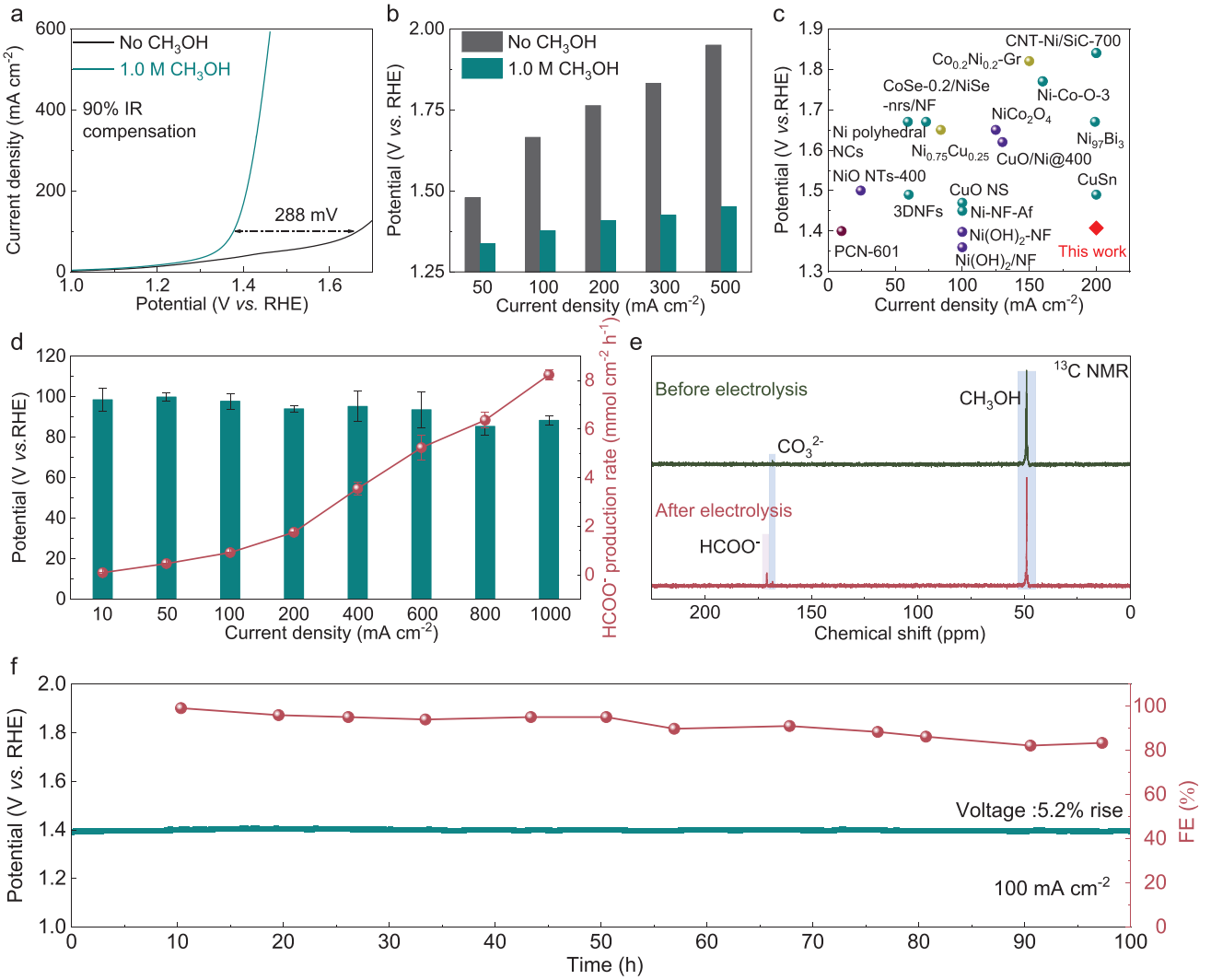

Figure 3. Electrocatalytic performance of Cu—CuO—Cu_2O NWs catalyst for MOR. a) Linear sweep voltammetry (LSV) curves of Cu—CuO—Cu_2O NWs in 1.0 M KOH electrolyte with and without 1.0 M CH_3OH. b) Anodic potentials at varied current densities (50, 100, 200, 300, and 500 mA cm^{-2}) in 1.0 M KOH electrolyte with and without 1.0 M methanol by using Cu—CuO—Cu_2O NWs. c) The catalytic activity comparison of the Cu—CuO—Cu_2O NWs with the reported high-performance MOR catalysts. d) FE and production rate of $HCOO^-$ obtained at different current densities in 1.0 M KOH electrolyte with 1.0 M methanol. e) ^{13}C NMR spectra for the 1.0 M KOH + 1.0 M methanol electrolyte before and after 2 h continuous electrolysis at 100 mA cm^{-2}. f) Chronopotentiometry experiment profile and FEs at a current density of 100 mA cm^{-2} for long-term stability testing.

the intensity and area of this peak remain unchanged, indicating no over-oxidation happens during the MOR process. Moreover, a prominent $HCOO^-$ signal (171.1 ppm) becomes visible, indicating that the catalyst exhibits high selectivity for the four-electron MOR.[22]

We then directed our focus on assessing the stability of the catalyst for MOR. To mitigate the influences of CH_3OH depletion and $HCOO^-$ accumulation, we conducted extended operations at a current density of 100 mA cm^{-2} in a continuous electrolyte flow system (Note S3, Supporting Information). As shown in Figure 3f, the catalyst demonstrates exceptional stability with a high FE exceeding 90% during the initial 50 h of operation. Although a slight degradation is observed during the subsequent 50 h, the FE remains above 82%. Impressively, after 100 h of reaction, the potential only increased by 5.2%, making it one of the best-performing MOR catalysts reported to date compared to previously documented systems (Figure S14, Supporting Information).

2.3. Methanol Assists Surface Reconstruction of Catalyst for MOR

The exceptional performance of the Cu—CuO—Cu_2O NWs catalyst in the MOR has prompted us to explore any catalyst modifications that contribute to its high activity and unravel the underlying mechanisms involved. To begin with, we conducted an analysis of the catalyst's intrinsic properties, ruling out any significant changes. Examination of the SEM image and XRD pattern revealed no discernible alterations in morphology or the

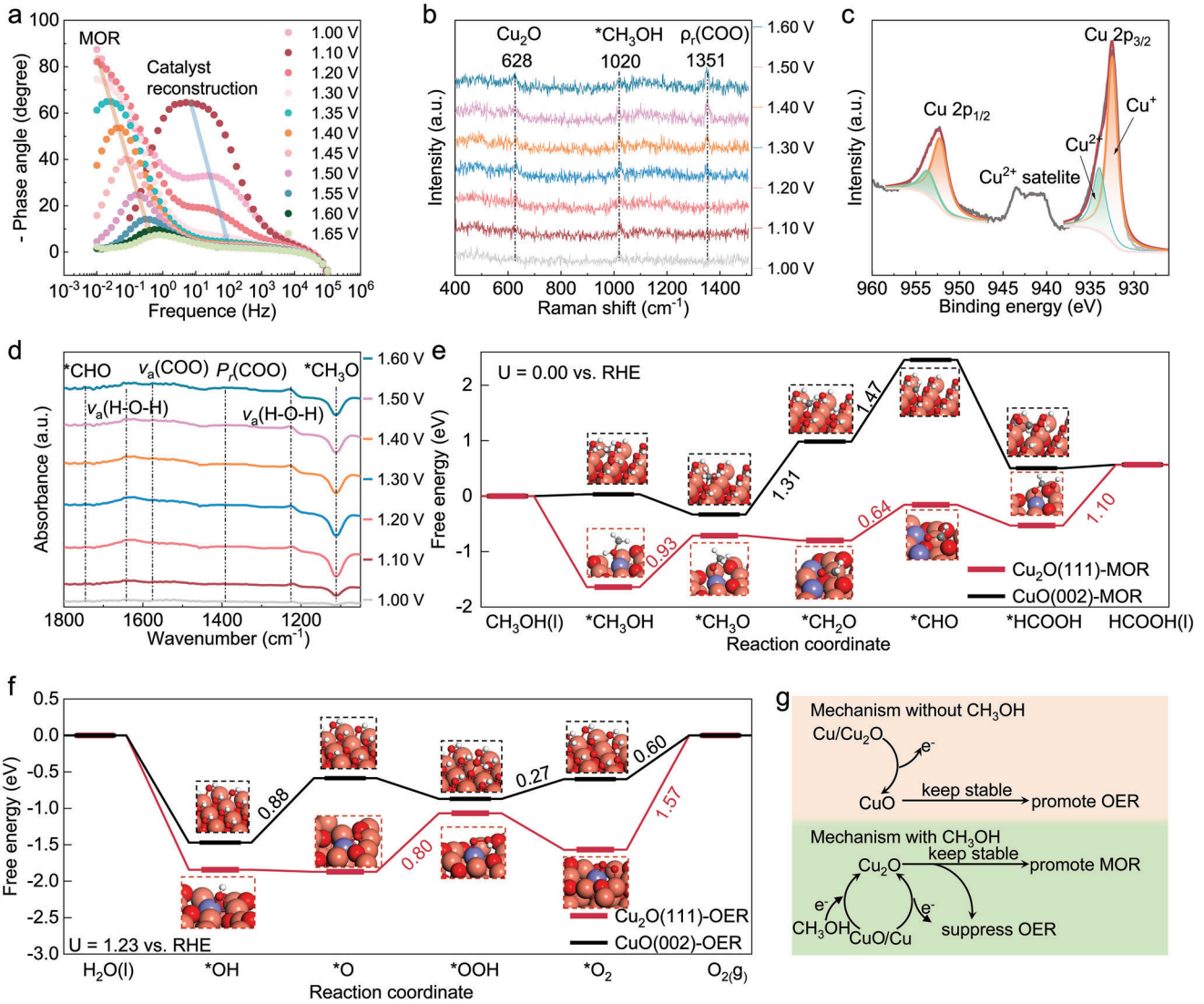

Figure 4. MOR promoting mechanism on Cu—CuO—Cu_2O NWs catalysts. a) Bode phase plots of the in situ EIS on Cu—CuO—Cu_2O NWs catalyst in 1.0 M KOH with 1.0 M CH_3OH. b) Operando Raman spectra for the Cu—CuO—Cu_2O NWs at various potentials in 1.0 M KOH with 1.0 M CH_3OH. c) Cu 2p XPS spectra of the Cu—CuO—Cu_2O NWs after 1 h reaction at 100 mA cm^{-2}. d) ATR-SEIRAS spectra during MOR in 1.0 M KOH containing 1.0 M methanol electrolyte. e) Free energy diagram for MOR proceeded on Cu_2O(111) and CuO(002) facets at 298.15K, U_{RHE} = 0.00 V. f) Free energy diagram for OER proceeded on Cu_2O(111) and CuO(002) facets at 298.15K, U_{RHE} = 1.23 V. g) Schematic diagram of MOR promoting mechanism on Cu—CuO—Cu_2O NWs catalysts.

appearance of new phases after the MOR reaction (Figure S15, Supporting Information).

Subsequently, we embarked on exploring the possibility of surface reconstruction of the catalyst during the electrochemical reaction. We first employed operando electrochemical impedance spectroscopy (OEIS) to simultaneously monitor the alterations occurring on the catalyst surface as well as the electrochemical processes involved in MOR and OER (**Figure** 4a; Figure S16, Supporting Information). Upon initial execution of the OEIS test in a 1.0 M KOH electrolyte, a solitary peak was detected at a low frequency, ascribed to the OER. In contrast, when the OEIS test was conducted in a 1.0 M CH_3OH + 1.0 M KOH electrolyte, two distinct peaks appeared. The peak at a lower frequency was associated with the MOR, while an additional peak at a higher frequency following 1.0 V indicates potential surface reconstruction during the electrocatalysis process. When the concentration of CH_3OH was decreased, this peak remained, implying that the catalyst construction process was not affected by the CH_3OH concentration (Figure S17, Supporting Information). Initially, we hypothesized that this change might be solely attributed to the oxidation of the Cu substrate, as a similar peak appeared at the same position when

Cu foam was used as the catalyst (Figure S18, Supporting Information). However, the in situ Raman spectroscopy specifically utilizing the NWWs also shows an increase in the Cu_2O signal with increasing potential (Figure 4b).[23] This observation differs when the electrolyte is devoid of CH_3OH (Figure S19, Supporting Information). Furthermore, the Cu 2p XPS analysis after the

MOR also indicated a significantly higher Cu^+ signal compared to the unreacted catalyst (Figure 4c,e), suggesting that some CuO may be transformed to Cu_2O. In addition, the catalyst surface presents the (111) plane of Cu_2O, which was previously occupied by the (002) plane of CuO, further supporting our findings (Figure S20, Supporting Information). Thus, we propose that the Cu_2O originates from the Cu substrate and surface CuO, acting as the active catalyst for promoting MOR. The conversion process is likely closely associated with the reducibility of aldehyde species ($^*CHO$),[24] an intermediate in the CH_3OH oxidation process. This intermediate can facilitate the conversion of high-valent metal cations into their low-valent counterparts. As demonstrated in the equation below, for Cu, the process may initially involve the oxidation of Cu to Cu^{2+}, followed by a reaction with OH^- to form $Cu(OH)_2$ (step 1). Subsequently, $Cu(OH)_2$ is reduced to Cu_2O, aided by the presence of $^*CHO$ (step 2). CuO undergoes a similar reduction process (step 3).

$$Cu + 2OH^- \rightarrow Cu(OH)_2 + 2e^- \quad (1)$$

$$2Cu(OH)_2 + * CHO \rightarrow Cu_2O + * COOH + 2H_2O \quad (2)$$

$$2CuO + * CHO \rightarrow Cu_2O + * COOH \quad (3)$$

Such unexpected phenomena motivated us to further investigate the MOR mechanism by in situ attenuated total reflectance surface-enhanced infrared absorption spectroscopy (ATR-SEIRAS) and theoretical calculation. In the in situ ATR-SEIRAS analysis performed in a 1.0 M KOH solution containing 1.0 M CH_3OH (Figure 4d), we observed the increasing intensity of server peaks in the spectra following the reaction potential increase. The band at ≈1574 cm^{-1} is assigned to ν_a(COO),[25] while the bands from 1300 to 1390 cm^{-1} are assigned to δ(CH)/ρ_r(COO) signal of $HCOO^-$.[26] The peaks at 1116 and 1574 cm^{-2} can be assigned to $^*CH_3O$ and $^*CHO$, respectively.[27] In addition, the band at 1220 and 1640 cm^{-1} can be assigned to water deformation.[28] Based on this result, we propose that the methanol oxidation pathway on the catalyst is $CH_3OH \rightarrow {}^*CH_3OH \rightarrow {}^*CH_3O \rightarrow {}^*CH_2O \rightarrow {}^*CHO \rightarrow {}^*HCOOH \rightarrow HCOOH$. In addition, the strong peak at 1351 cm^{-1} shown in Figure 4b also demonstrates the formation of the $HCOO^-$, which means the $^*CHO$ intermediate does not undergo further oxidation to cleavage the C—H bond and form CO_2 but interacts with OH^-.[29]

The density functional theory (DFT) calculations were further employed to explore the influence of catalyst reconstruction on the MOR processes. The models of Cu_2O(111) and CuO(002) facets are based on experimental characterizations (Figures S21–S24, Supporting Information, more details are given in the Computational Details Section). DFT+U calculations based on computational hydrogen electrode model (CHEM)[30] were performed to determine the free energy diagram for MOR and OER on Cu_2O(111) and CuO(002) facets (Figure 4e,f). For MOR, the predominant four-electron oxidation pathway[31] to produce formic acid as computed under U_{RHE} of 0.00 V. Figure 4e illustrates that $^*CH_3OH$ to $^*CH_3O$ is the rate-determining step (RDS) for Cu_2O(111) facet with ΔG of 0.93 eV, while $^*CH_2O$ to $^*CHO$ serves as the RDS for CuO(002) facet with much higher ΔG of 1.47 eV, indicating that the Cu_2O(111) facet presents better MOR performance than CuO(002) facet. We also note that the desorption of HCOOH on the Cu_2O(111) surface has ΔG as high as 1.10 eV, which may hinder the overall high rate. This step can actually be speeded up by accumulating HCOOH on the surface. Quantitatively, when the coverage is increased from 1/4 monolayer (ML) to 1/2 ML, 3/4 ML, and 1 ML (Figure S25, Supporting Information), the average desorption energies of HCOOH will decrease to +0.54, +0.34, and +0.16 eV, respectively. We consider the step of the desorption of O_2 . For OER, the four-electron pathway is performed under U_{RHE} = 1.23 V. Figure 4f displays that $^*O$ to $^*OOH$ and $^*OH$ to $^*O$ are the RDSs for Cu_2O(111) and CuO(002) facets, with similar ΔG of 0.80 and 0.88 eV, respectively. Different from the conventional OER process, affinity of copper oxide to oxygen. It is found that the desorption of O_2 on Cu_2O(111) facet is much harder than that on the CuO(002) facet (1.57 vs 0.60 eV). Moreover, the desorption energy of O_2 is still as high as 0.96 eV when O_2 coverage increases to 1ML (Figure S26, Supporting Information), thus such a large desorption energy on Cu_2O(111) facet origins from the strong interaction between O_2 and Cu_{1c} and is slightly impacted by O_2 coverage. We speculate that the CuO(002) facet has better OER performance than Cu_2O(111) facet, owing to the formed O_2 being hard to desorb from Cu_2O(111) facet.

Based on the experiments and calculations, the promotional effects of the Cu—CuO—Cu_2O NWs on MOR are proposed (Figure 4g). Methanol in the electrolyte not only acts as a reactant but also participates in the reconstruction of the catalyst surface, facilitating a transition from Cu/CuO to Cu_2O and ensuring its stability. The surface Cu_2O alters the rate-determining step (RDS), requiring significantly less energy than the original CuO surface to enhance the MOR. Additionally, the competitive O_2 evolution process is suppressed due to the challenging desorption of O_2 on the Cu_2O surface.

2.4. Integration of Cathodic CO_2RR and Anodic MOR for Continuous $HCOO^-$ Production with Nearly 200% Efficiency

Prior to the assembly of the coupling cell, a cathodic bismuth nanosheet (Bi NS) catalyst was prepared following a previously reported method.[32] The as-prepared Bi NS shows a distinctive 2D lamellar structure with a uniform distribution of Bi element, (Figure S27, Supporting Information and the inset of **Figure 5a**). As an efficient catalyst for electrochemical reduction of CO_2 to $HCOO^-$, the Bi NS exhibits an impressively low potential of −0.65 V versus RHE under a reduction current of 10 mA cm^{-2} at in 0.5 M $KHCO_3$ electrolyte (Figure 5a). Additionally, the Bi NS consistently exhibited a high FE of over 90% across a wide range of potentials (Figure S28, Supporting Information). To accurately determine the FE, we employed a newly developed calibration curve specifically tested in a 0.5 M $KHCO_3$ electrolyte to minimize the influence of the electrolyte composition[33] (Figure S29, Supporting Information). Such distinctive features render Bi NS well-suited for subsequent coupling procedures and ensure efficient electron utilization. Moreover, to demonstrate the feasibility of the couple reaction, we further evaluated the performance of our anode catalyst in a three-electrode flow cell, which is more practically available. As shown in Figure S30a (Supporting Information), the observed MOR activity was slightly lower compared

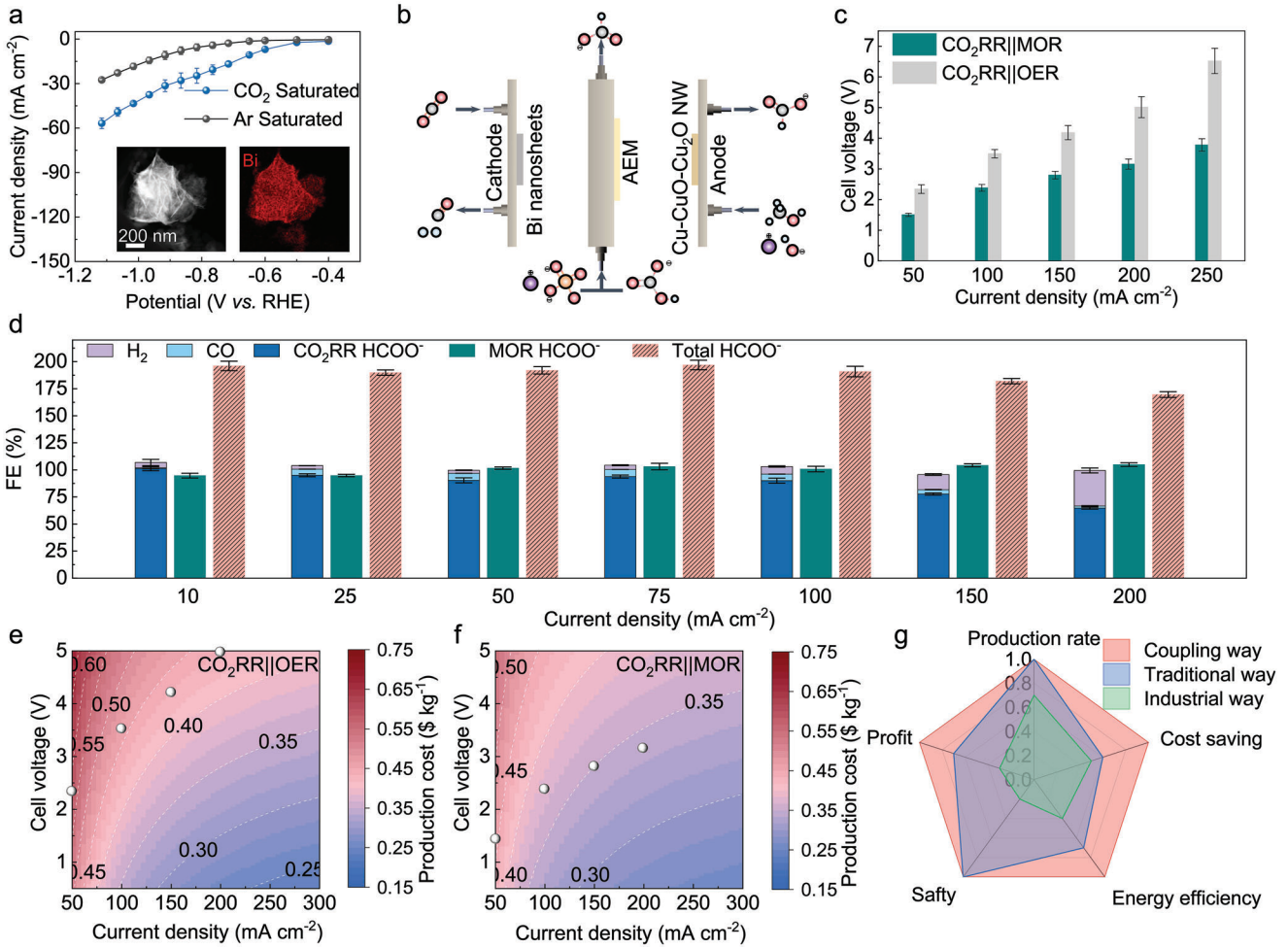

Figure 5. Electrocatalytic performance of the coupling cell. a) The I-V curve of Bi NS catalysts in Ar or CO_2 saturated electrolytes, the insets are the scanning transmission electron microscope – energy dispersive X-ray (STEM-EDX) images of the prepared Bi NS catalysts. b) A schematic illustration shows the flow cell, which couples CO_2RR at the cathode with MOR at the anode, separated by the AEM (gray balls: C atoms, blue balls: H atoms, orange balls: S atoms, purple balls: K atoms). c) Cell voltage comparison in coupling cell and traditional flow cell at different current densities. d) FE of $HCOO^-$ obtained at different current densities by using the coupling cell. $HCOO^-$ production cost with cell voltage and current density as variables in e) coupling cell and f) traditional flow cell, the white point is the estimated cost according to the tested results. g) A radar plot comparison of different $HCOO^-$ production technologies.

to that in an H-type cell, achieving 100 mA cm^{-2} at 1.397 V. This variation in activity could be attributed to the mass transfer differences of the flowing electrolyte. The presence of bubbles might prevent the entire catalytic area from establishing direct contact with the liquid, resulting in a lower current density compared to what is achieved in an H-type cell at the same potential. The selectivity testing results were consistent with those from the H-type cell (Figure S30b, Supporting Information), notably reaching an outstanding FE of 97% at 100 mA cm^{-2}.

Aiming to boost the production rate and maximize electron utilization efficiency, we then assembled a two-electrode flow cell integrating the MOR and CO_2RR processes, utilizing the high-performance Cu—CuO—Cu_2O NWs and Bi NS catalysts, respectively (Figure 5b). An anolyte consisted of 1.0 M KOH + 1.0 M CH_3OH, while the catholyte comprised of 0.5 M $KHCO_3$ + 0.25 M K_2SO_4, ensuring high ionic conductivity. A gas diffusion electrode (GDE) was employed to overcome the mass diffusion limitation of CO_2 at the cathode, and an anion exchange membrane (AEM) was used to separate the cathode and anode. Figure 5c compares the cell voltage under different reaction conditions, highlighting the significant role of the anodic reaction in controlling the overall reactions. The replacement of the OER with MOR results in a substantial decrease in cell voltage, significantly reducing the energy consumption for $HCOO^-$ production. At a current density of 100 mA cm^{-2}, the CO_2RR||MOR exhibits a cell voltage of 2.382 V versus RHE, which is 1.114 V lower than the CO_2RR||OER configuration, the energy consumption of the coupling cell is only 68.1% of the tradition way, and this value decreased further to 59.0% when the current density increases to 200 mA cm^{-2} (Figure S31, Supporting Information). Furthermore, our coupled cell also demonstrated a high FE for $HCOO^-$ production, nearly reaching 200%. Specifically, the cell achieves FE values of 197%, 191%, and 182% at 75, 100, and 150 mA cm^{-2}, respectively (Figure 5d). High

production rates of 2.62 and 3.63 mmol cm^{-2} h^{-1} (28.93 and 40.08 kg m^{-2} day^{-1}) were achieved at 100 and 150 mA cm^{-2}, respectively (Figure S32, Supporting Information). Interestingly, the anode FE exceeds 100% at a current density range of 50–200 mA cm^{-2} (Figure 5d), which might be attributed to the transport of some $HCOO^-$ produced at the cathode through the AEM to the anode. This process slightly reduces the overall FE due to the two-electron process involved in CO_2RR for $HCOO^-$ production, whereas the MOR requires a four-electron process. Following this, we conducted a stability examination. The results are depicted in Figure S33 (Supporting Information). Intriguingly, there was minimal variation in the cell voltage after 6-hour electrolysis at a current density of 100 mA cm^{-2}. However, a decrease in the overall FE to 180% was observed, primarily attributed to a reduction in the cathode's FE. The primary factor for this reduction in cathode FE is theorized to be an accretion of carbonate in the flow channel, coupled with flooding issues of the gas diffusion layer.

Furthermore, we conducted a comprehensive techno-economic analysis based on our data, considering various cell configurations and evaluating production cost and potential profit. The analysis revealed that the coupled cell configuration offers significantly lower product costs compared to traditional independent cells (Figure 5e,f). At current densities of 100 and 150 mA cm^{-2}, the cost in a coupled cell is ≈0.37 and 0.35 \$ kg^{-1}, while traditional independent cells require 0.47 and 0.43 \$ kg^{-1}. Moreover, the estimated yearly profit demonstrates that the traditional method can only yield 59% of the profit achieved by the coupled method at 100 mA cm^{-2} and less than half at 150 and 200 mA cm^{-2} (Figure S34a, Supporting Information). Considering the net present value over 20 years, the traditional method appears unprofitable, while the coupled method can generate a profit of over 10 million when the current density exceeds 100 mA cm^{-2} (Figure S34b, Supporting Information). Our analysis thus illustrates that the coupled system holds several advantages over traditional and industrial methods by using high-performance Cu—CuO—Cu_2O NWs, including enhanced energy efficiency, cost savings, increased product rate, higher profit, and improved safety.

3. Conclusion

We have successfully synthesized a high-efficiency Cu—CuO—Cu_2O NWs catalyst that demonstrates remarkable performance in MOR, achieving an $FE_{(HCOO^-)}$ near 100% over a broad current density range from 100 to 600 mA cm^{-2} while also exhibiting outstanding longevity, remaining stable over 100 h at a current density of 100 mA cm^{-2}. Notably, we uncover the crucial role of methanol in facilitating a surface reconfiguration of the catalyst, resulting in the transformation of the Cu substrate and surface CuO into Cu_2O. This metamorphosis enhances the four-electron MOR while inhibiting the competing OER. To fully harness the potential of our Cu—CuO—Cu_2O NWs catalyst, we develop a coupling catalysis system by integrating it as the anode catalyst with an efficient cathodic CO_2RR. This integrated system achieves an impressive faradaic efficiency of close to 200% at a low cell voltage of 2.382 V operating at 100 mA cm^{-2} and substantial production rates of 28.93 and 40.08 kg m^{-2} day^{-1} at 100 and 150 mA cm^{-2}, respectively. Our techno-economic evaluation projects the production costs of HCOOH at ≈US\$0.37 and 0.35 kg^{-1} at 100 and 150 mA cm^{-2}, respectively, representing substantial improvements over conventional electrochemical methodologies. We anticipate that our study will accelerate the development and implementation of integrated systems for efficient and cost-effective $HCOO^-$ production, fostering advancements in sustainable energy technologies.

Supporting Information

Supporting Information is available from the Wiley Online Library or from the author.

Acknowledgements

X.Z. acknowledges the support from the Hong Kong Polytechnic University (CD9B and WZ4Q), the National Natural Science Foundation of China (22205187), and the Shenzhen Municipal Science and Technology Innovation Commission (R2023A045). C.C.L. acknowledges the support from the National Science and Technology Council of Taiwan (contract nos. NSTC 111-2113-M-027-005-MY2 and NSTC 112-2622-M-027-001), and NSRRC TLS 01C and 17C.

Conflict of Interest

The authors declare no conflict of interest.

Data Availability Statement

The data that support the findings of this study are available from the corresponding author upon reasonable request.

Keywords

coupling reaction, Cu-based catalysts, flow cell, methanol oxidation, surface reconstruction

Received: November 20, 2023
Revised: January 5, 2024
Published online: March 30, 2024

[1] a) H. Shin, K. U. Hansen, F. Jiao, *Nat. Sustain.* **2021**, *4*, 911; b) F. M. Jin, J. Yun, G. M. Li, A. Kishita, K. Tohji, H. J. Enomoto, *Green Chem.* **2008**, *10*, 612.
[2] a) F. Valentini, A. Marrocchi, L. Vaccaro, *Adv. Energy Mater.* **2022**, *12*, 2103362; b) F. Valentini, V. Kozell, C. Petrucci, A. Marrocchi, Y. L. Gu, D. Gelman, L. Vaccaro, *Energy Environ. Sci.* **2019**, *12*, 2646.
[3] P. Lanzafame, S. Abate, C. Ampelli, C. Genovese, R. Passalacqua, G. Centi, S. Perathoner, *ChemSusChem* **2017**, *10*, 4409.
[4] a) J. M. Spurgeon, N. Theaker, C. A. Phipps, S. S. Uttarwar, C. A. Grapperhaus, *ACS Sustainable Chem. Eng.* **2022**, *10*, 12882; b) J. P. Sheets, A. Shah, *Biofuels, Bioproducts and Biorefining* **2018**, *12*, 412.
[5] a) Q. Xia, K. E. Zhang, T. T. Zheng, L. An, C. Xia, X. Zhang, *ACS Energy Lett.* **2023**, *8*, 2840; b) D. A. Salvatore, C. M. Gabardo, A. Reyes, C. P. O'Brien, S. Holdcroft, P. Pintauro, B. Bahar, M. A. Hickner, C. Bae, D. Sinton, *Nat. Energy* **2021**, *6*, 339.

[6] a) T. T. Zheng, C. X. Liu, C. X. Guo, M. L. Zhang, X. Li, Q. Jiang, W. Q. Xue, H. L. Li, A. Li, C. W. Pao, *Nat. Nanotechnol.* **2021**, *16*, 1386; b) S. Dey, F. Masero, E. Brack, M. Fontecave, V. Mougel, *Nature* **2022**, *607*, 499.

[7] a) Y. Zang, D. Q. Lu, K. Wang, B. Li, P. Peng, Y. Q. Lan, S. Q. Zang, *Nat. Commun.* **2023**, *14*, 1792; b) G. D. Li, G. Q. Han, L. Wang, X. Y. Cui, N. K. Moehring, P. R. Kidambi, D. E. Jiang, Y. J. Sun, *Nat. Commun.* **2023**, *14*, 525; c) I. Roger, M. A. Shipman, M. D. Symes, *Nat. Rev. Chem* **2017**, *1*, 0003.

[8] a) Y. Li, X. F. Wei, L. S. Chen, J. L. Shi, M. Y. He, *Nat. Commun.* **2019**, *10*, 5335. b) R. Navarro, M. Sanchez-Sanchez, M. Alvarez-Galvan, F. Del Valle, J. Fierro, *Energy Environ. Sci.* **2009**, *2*, 35.

[9] a) B. T. Zhu, B. Dong, F. Wang, Q. F. Yang, Y. P. He, C. J. Zhang, P. Jin, L. Feng, *Nat. Commun.* **2023**, *14*, 1686. b) Z. W. Chang, F. T. Kong, M. Wang, S. H. Han, X. Z. Cui, H. Tian, Y. F. Chen, G. Meng, C. Chen, Y. Liu, *Chem. Catal.* **2022**, *2*, 358.

[10] a) X. F. Wei, Y. Li, L. S. Chen, J. L. Shi, *Angew. Chem., Int. Ed.* **2021**, *60*, 3148; b) Y. Li, C. Z. Huo, H. J. Wang, Z. X. Ye, P. P. Luo, X. X. Cao, T. B. Lu, *Nano Energy* **2022**, *98*, 107277.

[11] a) M. Li, X. H. Deng, K. Xiang, Y. Liang, B. Zhao, J. Hao, J. L. Luo, X. Z. Fu, *ChemSusChem* **2020**, *13*, 914. b) J. S. Li, R. L. Wei, X. Wang, Y. Zuo, X. Han, J. D. Arbiol, J. Llorca, Y. Y. Yang, A. Cabot, C. H. Cui, *Angew. Chem., Int. Ed.* **2020**, *132*, 21012.

[12] a) J. Hao, J. W. Liu, D. Wu, M. X. Chen, Y. Liang, Q. Wang, L. Wang, X. Z. Fu, J. L. Luo, *Appl. Catal. B* **2021**, *281*, 119510; b) F. X. Meng, C. C. Dai, Z. Liu, S. Z. Luo, J. J. Ge, Y. Duan, G. Chen, C. Wei, R. R. Chen, J. R. Wang, *eScience* **2022**, *2*, 87; c) A. R. Silva Olaya, F. Kühling, C. Mahr, B. Zandersons, A. Rosenauer, J. Weissmüller, G. Wittstock, *ACS Catal.* **2022**, *12*, 4415.

[13] a) C. S. Cao, D. D. Ma, J. C. Jia, Q. Xu, X. T. Wu, Q. L. Zhu, *Adv. Mater.* **2021**, *33*, 2008631; b) Y. W. Zhou, Y. F. Chen, K. Jiang, Z. Liu, Z. J. Mao, W. Y. Zhang, W. F. Lin, W. B. Cai, *Appl. Catal. B* **2021**, *280*, 119393.

[14] S. Sakong, A. Gross, *J. Phys. Chem. A* **2007**, *111*, 8814.

[15] A. Hartmann, M. Puchert, R. Lamb, *Surf. Interface Anal.* **1996**, *24*, 671.

[16] C. W. Yang, X. J. Yu, S. Heißler, A. Nefedov, S. Colussi, J. Llorca, A. Trovarelli, Y. M. Wang, C. Wöll, *Angew. Chem., Int. Ed.* **2017**, *56*, 375.

[17] Q. M. Liu, Y. Peng, Z. Masood, D. DuBois, J. Tressel, F. Nichols, P. Ashby, R. Mercado, T. Assafa, D. J. Pan, *Adv. Mater.* **2023**, *35*, 2208665.

[18] a) G. T. Bae, *Comput. Theor. Chem.* **2021**, *1204*, 113377; b) S. Saedy, M. A. Newton, M. Zabilskiy, J. H. Lee, F. Krumeich, M. Ranocchiari, J. A. van Bokhoven, *Catal. Sci. Technol.* **2022**, *12*, 2703.

[19] B. Ipek, M. J. Wulfers, H. Kim, F. Goltl, I. Hermans, J. P. Smith, K. S. Booksh, C. M. Brown, R. F. Lobo, *ACS Catal.* **2017**, *7*, 4291.

[20] a) Y. B. Qi, Y. Zhang, L. Yang, Y. H. Zhao, Y. H. Zhu, H. L. Jiang, C. Z. Li, *Nat. Commun.* **2022**, *13*, 4602; b) A. A. Dubale, Y. Y. Zheng, H. L. Wang, R. Hübner, Y. Li, J. Yang, J. W. Zhang, N. K. Sethi, L. Q. He, Z. K. Zheng, *Angew. Chem., Int. Ed.* **2020**, *59*, 13891; c) M. R. Zhang, J. P. Zhu, R. Wan, B. Liu, D. D. Zhang, C. Zhang, J. P. Wang, J. Y. Niu, *Chem. Mater.* **2022**, *34*, 959.

[21] a) J. S. Li, Y. Zuo, J. F. Liu, X. Wang, X. T. Yu, R. F. Du, T. Zhang, M. F. Infante-Carrió, P. Y. Tang, J. D. Arbiol, *J. Mater. Chem. A* **2019**, *7*, 22036; b) S. N. Sun, L. Z. Dong, J. R. Li, J. W. Shi, J. Liu, Y. R. Wang, Q. Huang, Y. Q. Lan, *Angew. Chem., Int. Ed.* **2022**, *134*, 202207282; c) T. J. Wang, H. Huang, X. R. Wu, H. C. Yao, F. M. Li, P. Chen, P. J. Jin, Z. W. Deng, Y. Chen, *Nanoscale* **2019**, *11*, 19783; d) X. G. Guo, T. T. Liang, D. X. Zhang, M. Z. Zhang, Y. H. Lin, C. Lai, *Mater. Chem. Phys.* **2019**, *221*, 390; e) B. Q. Yang, Y. W. Yu, J. Y. Qiao, L. F. Yuan, X. D. Shen, X. L. Hu, *Appl. Surf. Sci.* **2020**, *513*, 145808; f) J. N. Du, S. J. You, X. R. Li, B. Tang, B. J. Jiang, Y. Yu, Z. Cai, N. Q. Ren, J. L. Zou, *ACS Appl. Mater. Interfaces* **2019**, *12*, 686; g) S. Chen, D. M. Huang, D. Y. Liu, H. Z. Sun, W. J. Yan, J. C. Wang, M. Dong, X. L. Tong, W. B. Fan, *Appl. Catal. B* **2021**, *291*, 120065; h) B. Baruah, A. Kumar, in *Ceramic and Specialty Electrolytes for Energy Storage Devices*, CRC Press, Boca Raton, Florida, USA **2021**; i) P. Arunachalam, M. A. Ghanem, A. M. Al-Mayouf, M. Al-shalwi, *Mater. Lett.* **2017**, *196*, 365; j) A. A. Dubale, Y. Zheng, H. Wang, R. Hubner, Y. Li, J. Yang, J. Zhang, N. K. Sethi, L. He, Z. Zheng, W. Liu, *Angew. Chem., Int. Ed.* **2020**, *59*, 13891; k) R. H. Que, M. L. Li, H. Yao, X. H. Wang, F. Liao, M. W. Shao, *ChemSusChem* **2020**, *13*, 964; l) S. Xie, X. L. Tong, G. Q. Jin, Y. Qin, X. Y. Guo, *J. Mater. Chem. A* **2013**, *1*, 2104.

[22] Y. R. Wang, H. M. Ding, S. N. Sun, J. W. Shi, Y. L. Yang, Q. Li, Y. F. Chen, S. L. Li, Y. Q. Lan, *Angew. Chem., Int. Ed.* **2022**, *61*, 202212162.

[23] Y. L. Deng, A. D. Handoko, Y. H. Du, S. B. Xi, B. S. Yeo, *ACS Catal.* **2016**, *6*, 2473.

[24] Y. Q. Zhang, B. Zhou, Z. X. Wei, W. Zhou, D. D. Wang, J. Tian, T. H. Wang, S. L. Zhao, J. L. Liu, L. Tao, *Adv. Mater.* **2021**, *33*, 2104791.

[25] P. Christensen, D. Linares-Moya, *J. Phys. Chem. C* **2010**, *114*, 1094.

[26] A. Kowal, S. N. Port, R. J. Nichols, *Catal. Today* **1997**, *38*, 483.

[27] a) M. Sun, L. X. Zhang, F. L. Tian, J. X. Li, Y. Q. Lei, H. Zhang, L. F. Han, Z. H. Guo, Y. H. Gao, F. R. Liu, *J. Energy Chem.* **2024**, *88*, 521; b) S. H. Chen, W. H. Li, W. J. Jiang, J. R. Yang, J. X. Zhu, L. Q. Wang, H. H. Ou, Z. Z. Zhuang, M. Z. Chen, X. H. Sun, *Angew. Chem. Int. Ed. Engl.* **2022**, *134*, 202114450.

[28] L. L. Liao, G. M. Xia, F. Q. Yu, X. Liu, M. X. Shu, G. Y. Zhang, X. S. Zeng, H. M. Wang, *Small* **2023**, *19*, 2300926.

[29] W. Huang, Z. Li, Y. Peng, S. Chen, J. Zheng, Z. Niu, *J. Solid State Electrochem.* **2005**, *9*, 284.

[30] J. K. Nørskov, T. Bligaard, A. Logadottir, J. Kitchin, J. G. Chen, S. Pandelov, U. Stimming, *J. Electrochem. Soc.* **2005**, *152*, J23.

[31] B. Zhu, B. Dong, F. Wang, Q. Yang, Y. He, C. Zhang, P. Jin, L. Feng, *Nat. Commun.* **2023**, *14*, 1686.

[32] C. Xia, P. Zhu, Q. Jiang, Y. Pan, W. T. Liang, E. Stavitski, H. N. Alshareef, H. T. Wang, *Nat. Energy* **2019**, *4*, 776.

[33] a) A. Sasikumar, J. M. Griffin, C. Merlet, *J. Phys. Chem. Lett.* **2022**, *13*, 8953; b) A. Blaskó, C. A. Bunton, S. Bunel, C. Ibarra, E. Moraga, *Carbohydr. Res.* **1997**, *298*, 163.